Coloring 3D Printed Surfaces by Thermoforming

Yizhong Zhang, *Student Member, IEEE,* Yiying Tong, *Member, IEEE,* and Kun Zhou, *Fellow, IEEE*

Abstract—Decorating the surfaces of 3D printed objects with color textures is still not readily available in most consumer-level or even high-end 3D printers. Existing techniques such as hydrographics color transfer suffer from the issues of air pockets in concave regions and discoloration in overly stretched regions. We propose a novel thermoforming-based coloring technique to alleviate these problems as well as to simplify the overall procedure. Thermoforming is a widely used technique in industry for plastic thin shell product manufacturing by pressing heated plastic sheets onto molds using atmospheric pressure. We attach on the transparent plastic sheet a precomputed color pattern decal prior to heating, and adhere it to 3D printed models treated as the molds in thermoforming. The 3D models are thus decorated with the desired color texture, as well as a thin, polished protective cover. The precomputation involves a physical simulation of the thermoforming process to compute the correct color pattern on the plastic sheet, and the vent hole layout on the 3D model for air pocket elimination. We demonstrate the effectiveness and accuracy of our computational model and our prototype thermoforming surface coloring system through physical experiments.

Index Terms—3D printing, thermoforming, thermoplastic sheet simulation, texture mapping

1 Introduction

The past few years have witnessed a rapid increase in the popularity of 3D printing, e.g., for fast prototyping. However, coloring the surface of the printed model remains challenging, especially for concave regions. While high-end 3D printers do provide the possibility of printing the 3D model with colored surface, most of them use limited materials, and are slow and costly to produce the desired appearance. The state-of-the-art computational hydrographic printing allows the decoration of the surface after the 3D printing is done (e.g., [1], [2]). However, such methods still have difficulties in covering highly concave regions.

We propose a simple, yet effective approach to coloring the surface of 3D printed models by thermoforming a thin plastic sheet with texture to adhere seamlessly onto the surface. Thermoforming deforms a heated plastic sheet into the shape specified by the mold. The sheet is heated into a pliable working temperature, stretched into the mold, cooled down in the finished shape, and trimmed into commonly used products, ranging from thin-gauge disposable packaging to heavy-gauge aircraft screens. There are different techniques to press the sheet against the mold, including the popular vacuum forming, dating back to the 1940s. For our surface coloring application, an off-the-shelf thin-gauge vacuum forming serves the purpose. Fig. 1 illustrates the typical process of vacuum forming (also see the supplementary video).

In order to deliver the desired texture on the final shape in thermoforming, manual or vision-based techniques are often used to pre-distort the image pattern on the colored sheet prior to forming. Such techniques require repeated thermoforming to achieve the desired texture, which can be costly unless used in mass production. For customized

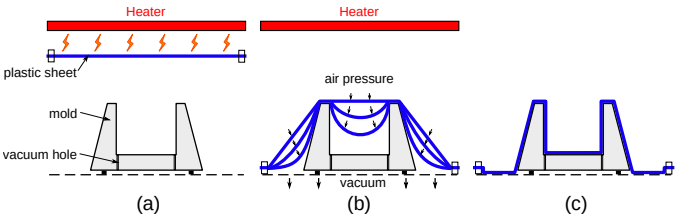

Fig. 1. A typical process of vacuum forming. (a) A plastic sheet is heated until soft enough for forming. (b) Then it is loaded to the mold; upon touching the mold, it begins to deform. As the air in the space below is vacuumed, the atmospheric air pressure forces the plastic sheet to conform to the mold surface. (c) After cooling down, the plastic is hardened into the new shape.

3D printed objects, we, instead, propose to use virtual simulation to perform the color alignment, as done in computational hydrographics. As thin thermoforming sheets stretch more evenly than the material for hydrographics color transfer, our simulation produces more reliable and accurate results in regions with large stretching. More importantly, during our simulation, we also tackle the difficulty with concave regions by an automatic strategic placement of vacuum holes to eliminate the air pockets for airtight contact between the sheet and the surface.

Our physical experiments using a low-end thermoforming machine demonstrate the potential of our system. Once we estimate the parameters of the thin plastic sheets we use, we apply the same simulation and air pocket treatment algorithms on various models, with and without large concave regions, and are able to replicate the rendered appearances of these textured 3D models. Such an easily accessible system would provide an additional incentive for additive manufacturing, the ability to decorate 3D printed shapes with a cosmetic layer for desired color pattern at low cost. Our technique can also be regarded as a fast prototyping tool for designs in industrial applications.

Our main contributions include:

- an accurate, easy-to-tune physical simulator specifically

- *Y. Zhang and K. Zhou are with the State Key Lab of CAD&CG, Zhejiang University, Mengminwei Building, Zijingang Campus, Hangzhou, Zhejiang, China 310058. E-mail: yizhongzhang1989@gmail.com, kunzhou@acm.org.*
- *Y. Tong is with Computer Science and Engineering Department, Michigan State University, 428 S. Shaw Lane Rm 3115, East Lansing, MI 48840. E-mail: ytong@msu.edu*

designed for thermoforming,
- an automatic vacuum hole placement algorithm based on the topological changes of air pockets during the deformation,
- and an end-to-end prototype system from the prewarping of texture based on physical simulation, printing of colored sheet, 3D printing of the vented model, to thermoforming of the sheet onto the 3D model.

2 Related Work

3D Printing. As additive manufacturing, or 3D printing technology matured, there has been a surge of methods for customizing the desired physical properties of the solid volume (e.g., [3], [4], [5], [6], [7], [8], [9], [10], [11], [12], [13]. Techniques have also been proposed to develop a thin layer of material with desired reflectance properties by mixing heterogeneous materials, surpassing the regular RGB color printing (e.g., [14], [15], [16], [17], [18], [19]. However, these methods do not provide insights on affordable full-color printing of a textured 3D model.

Surface Coloring. While it is possible to directly print the textured 3D models with high-end 3D printers, or with additional techniques such plating or enameling [20], [21], such procedures are not only costly but also with limitations on the target model material or choices on colors. Vinyl decals [22] and hydrographics provide techniques that are hard to control the precise locations of the pixels on curved surfaces. The most successful affordable approaches so far include computational hydrographic printing [1] and texture mapping real-world objects with hydrographics [2]. Both transfer pigments printed on a flat sheet onto curved surfaces with a technique called hydrographics, both minimize the distortion of the desired appearance through prewarping of the texture based on simulated deformation of the sheet as it is attached to the surface, and both suffer from the air pockets formed during the transfer onto concave regions. Our method is designed to tackle the problem of air pockets in these regions while offering a simpler and "dry" overall procedure.

Thermoforming. We address the issue of air pockets by resorting to a different technique, thermoforming, which, by design, exhaust air from the space between the color sheet and the surface. As thermoforming has been a mature plastic fabrication technique widely used in industry for decades (see, e.g., the textbook on thermoforming [23]), we only review the most related methods. Using 3D printing as rapid tooling for thermoforming molds has been proposed in, e.g., [24]. However, the method does not address the issue of surface coloring, and it requires human intervention in designing the whole mold, including the layout of vacuum holes.

There are also existing methods for image pre-distortion based on computer vision (e.g., [25], [26]). However, such methods would have to physically perform the thermoforming for individual shapes. For large customized models, the prototyping can be costly and slow, with results at the mercy of the accuracy of vision registration methods and the ink used. Most inks would change intensity under distortion in thermoforming [27]. In contrast, our method does not require a physical experiment with each shape. Once the parameters of a type of thin sheet and a thermoforming machine are determined, it can be used to decorate any shapes, as long as they fit into the effective regions of the machine. We can also pre-adjust the ink intensity as we demonstrate later, which is impossible prior to a virtual simulation.

Concurrent to our work, Schüller et al. [28] also introduced a method of producing colored 3D models by thermoforming. These two methods use the viscous thin-sheet model with linear elasticity in the membrane energy with added plasticity. The main differences are that their method includes bending energy and ours includes adhesion force calculation before vacuuming, but the simulation results are similar. Our method contains additionally an automatic vacuum hole layout algorithm, enabling proper handling of highly concave regions.

Virtual Simulation of Thermoforming. Commercial software T-Sim developed by Accuform Corporation [29] is designed to simulate the process of thermoforming, so that the usability of the mold can be evaluated before fabricated. While it provides various additional tools for thermoforming, such as plug assists, its treatment on image pre-distortion to provide better image alignment is severely limited. It lacks the capability of locating or even adding vacuum holes in the mold to reduce air pockets, provides no color adjustment technique to reduce color deviation due to stretch, and only takes a top view image instead of a texture atlas as input. We implement our simulation of heated plastic thin sheet under air pressure based on finite element methods, as done in [30], [31], [32]. The heated plastic sheet behaves both elastically and plastically, so viscous sheet simulations are inadequate. Following [33], we use hyperelastic material properties as the basis of our simulation of the sheet. Multiplicative volume-preserving plasticity has been used in volumetric simulation such as [34], [35] and in thin sheet simulation [36]. We adapt the multiplicative plasticity model to be area-preserving with a simplified simulation as bending can be ignored with the fixed boundary condition in vacuum forming [30] and neither fracture nor tearing is present in the process. We further introduced a topological change tracking during the simulation, for the automatic vent hole layout determination based on concepts from computational topology [37].

3 Overview

The general idea of our method is to simulate the thermoforming process on the given textured shape before creating the physical model. The purpose of the simulation is to predistort the texture and locate the vent holes on the 3D model.

Fig. 2 shows the pipeline of our system, which includes the following steps:

1) **Virtual simulation.** We simulate how the plastic sheet collides with the model surface when softened by heat and lowered into vacuuming position, and how it adheres to the model surface under air pressure during vacuum forming.
2) **Color pattern computation.** Through simulation, we have obtained the mapping from the 3D model to the plastic sheet. When combined with texture mapping, we can produce the prewarped texture to print on the plastic

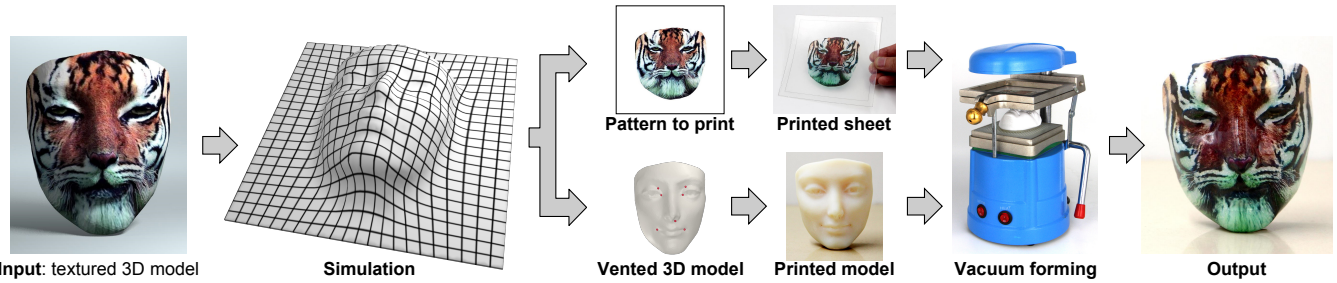

Fig. 2. The pipeline of our system. Our system takes a textured 3D digital model as input. By simulating the thermoforming process virtually, we can compute the correspondence map between the plastic sheet and the model surface, which will be used to calculate the pattern to print on the sheet. By tracking the motion of the plastic sheet, potential air pockets can be detected, which will be resolved by setting vacuum holes on the 3D model. Finally, the actual vacuum forming is performed using the plastic sheet with the printed color pattern and the 3D printed vented model on a vacuum forming machine. The final product is a 3D model decorated with the desired color texture.

sheet to achieve desired appearance after thermoforming.

3) **Vacuum hole placement.** In the vacuuming process, air pockets may form in concave regions of the mold, preventing the plastic sheet from adhering tightly to the surface. Based on the simulation, we detect potential air pockets by tracking topological changes of the cavities formed between the plastic sheet and the model, and then refine the 3D model by populating internal vacuum holes in optimal locations to eliminate the air pockets.
4) **Vacuum forming.** Finally, we carry out the physical process of thermoforming the color printed sheet onto the 3D printed model.

4 Simulation of Thermoforming

The main purpose of our thermoforming simulation is to determine the color pattern to print on the plastic sheet, so that the desired appearance will be attached to the surface of the 3D model. Thus, the key result is the correspondences between each pixel on the sheet and the surface point that it attaches to by the end of the simulation.

4.1 Thermoplastic Sheet

The sheets used in thermoforming are made of thermoplastics, i.e., polymers that become stretchable above a threshold temperature and solidify after cooling down. The constitutive relation of thermoplastics after being heated to working temperature is a plasticity model, whose stress-strain curve is similar to the one shown in Fig. 3(a). The turning point in the curve is the initial yield point, past which the deformation of the material includes a plastic part, and may not return to the original rest shape. After plastic deformation begins, the yield stress continues to increase due to work hardening. The stiffness of the material is also influenced by the strain rate (how fast the material is stretched), but its impact is low as mentioned in [38]. So we can ignore this effect in our simulation without introducing much error.

Our strain-rate independent elasto-plastic model is shown in Fig. 3(b). The yield stress is denoted as σ_0. When the von Mises stress of the material is below this threshold, it is just an elastic membrane strain model. Above σ_0, plasticity begins, and the material is work-hardened along with the

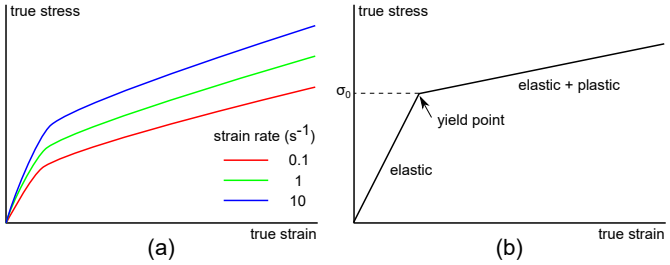

Fig. 3. (a) A typical physical true stress-true strain curve of thermoplastics. In the low stress range, the material behaves elastically. As the stress grows past the yield point, the material becomes plastic and the yield stress increases continuously due to work hardening. The relation is affected by strain rate, but the impact is low–10 times greater strain rate only results in 20% more stress. So we can safely assume constant strain rate during the simulation. (b) Our simplified stress-strain graph. The curve again behaves differently in two ranges of stress. Below the yield stress σ_0, the material undergoes elastic deformation only, whereas above σ_0 it undergoes elastic and plastic deformation.

stretch, leading to an increase in the yield strength. In this range, the material undergoes a combination of plastic and elastic deformation. Since the speed of elastic-plastic sheet deformation does not change the result by much, the model we use is independent of time and is solved in a quasi-static manner.

4.1.1 *Elasticity.*

The plastic sheets for thermoforming have thin-shell structures, but the heated polymer can be modeled as membrane since the bending strain is much smaller than the in-membrane stretching, as indicated in [30]. In fact, we did implement bending strain first, but with the fixed boundary condition, we found almost no difference in our test results, as shown in Fig. 4. So we simply omit bending strain for efficiency.

We use the membrane stress-strain relation proposed in [36]. With the natural 2D parametrization given by initial flat shape, the deformation gradient tensor $\boldsymbol{F}$ can be expressed as a 3×2 matrix. The Green's strain, which measures the in-membrane deformation, is given by

$$\boldsymbol{G} = \frac{1}{2}(\boldsymbol{F}^\top \boldsymbol{F} - \boldsymbol{I}), \tag{1}$$

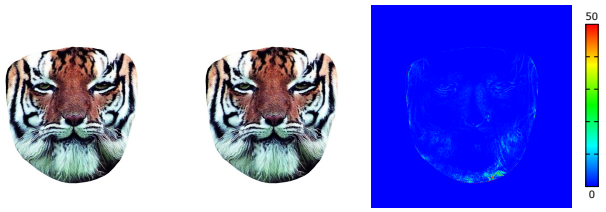

(a) (b) (c)

Fig. 4. The difference between images to be printed on the decal, simulated with and without bending strain energy: **(a)** with bending, **(b)** without bending, **(c)** and the difference showing the slight color deviation happening only within each pixel. Thus, we simply ignore bending strain during simulation for efficiency.

where $\boldsymbol{I}$ is the 2×2 identity matrix. The associated in-membrane stress is then calculated through

$$\boldsymbol{\sigma} = k_s((1-\nu)\boldsymbol{G} + \nu \mathrm{tr}(\boldsymbol{G})\boldsymbol{I}), \tag{2}$$

where $k_s = Yh/(1-\nu^2)$ is the stretching stiffness, Y is Young's modulus of the material, h is the sheet thickness and ν is Poisson's ratio (set to 0.5 for post-yield polymers[39]).

4.1.2 Plasticity.

The simulation of the plastic part of the deformation is modeled after [36] and [34]. We simplified their models since we are dealing with the quasi-static case, since we ignore the small influence of strain-rate on the results. In our membrane model, the deformation gradient $\boldsymbol{F}$ can be factorized into elastic part $\boldsymbol{F_e}$ and plastic part $\boldsymbol{F_p}$:

$$\boldsymbol{F} = \boldsymbol{F_e}\boldsymbol{F_p}, \tag{3}$$

which is similar to [34], except that in our curved 2D case, $\boldsymbol{F_e}$ is a 3×2 matrix, and $\boldsymbol{F_p}$ is a 2×2 matrix. In addition, we lifted the constraint $\det(\boldsymbol{F_p}) = 1$, because volume preservation is enforced through the change to the local sheet thickness h of each element.

In the beginning of simulation, $\boldsymbol{F_p}$ is set to identity, since no plastic deformation has occurred yet. As $\boldsymbol{F_p}$ evolves through plastic deformation as we describe next, the elastic deformation gradient $\boldsymbol{F_e}$ differs from total deformation gradient $\boldsymbol{F}$. In other words, $\boldsymbol{F_p}$ changed the rest shape of the membrane, so when computing Green's strain in Eq. (1) and the elastic stress in Eq. (2), $\boldsymbol{F_e}$ is used in place of $\boldsymbol{F}$.

At each simulation step, we examine whether the stress has exceeded the yield point by the von Mises criterion. The von Mises stress for in-membrane stress is

$$\sigma_v = \sqrt{\sigma_1^2 + \sigma_2^2 - \sigma_1\sigma_2} = \sqrt{(\mathrm{tr}\boldsymbol{\sigma})^2 - 3\,\det\boldsymbol{\sigma}}, \tag{4}$$

where σ_1 and σ_2 are the two eigenvalues of $\boldsymbol{\sigma}$ in Eq. (2). Once σ_v exceeds the initial yield stress σ_0, the material starts to undergo plastic deformation.

The plastic deformation further hardens the material, leading to an increase in the yield stress σ_y [40]. Assuming a linear hardening curve as in [32], the actual yield stress σ_y can be expressed as a function of $\boldsymbol{F_p}$, similar in form to the Ludwik's equation:

$$\sigma_y = \sigma_0 + K||\boldsymbol{F_p}^\top \boldsymbol{F_p} - \boldsymbol{I}||, \tag{5}$$

where σ_0 is the initial yield stress and K is the hardening coefficient controlling the slope of elastic-plastic range in Fig. 3(b).

The increment of σ_y will in turn raise the yield point, allowing the deforming to be elastic until $\sigma_v > \sigma_y$. In our quasi-static simulation, we assume that the hardening of the plastic is achieved within each time step, which requires that the von Mises stress to be lowered to the new yield stress, i.e., $\sigma_v = \sigma_y$, in each step, to reach perfect plastic effects [41]. We obtain this equilibrium by modifying the plastic deformation gradient $\boldsymbol{F_p}$, so that with the actual deformation gradient $\boldsymbol{F}$ fixed, the elastic part $\boldsymbol{F_e} = \boldsymbol{F}\boldsymbol{F_p}^{-1}$ changes to reduce σ_v, similar to the update used in [36], [34].

As the update to the plastic deformation gradient is based on reducing the strain, i.e., reducing the deviation of the principal stretches of $\boldsymbol{F_e}$ from 1, we first evaluate the principal stretches, by singular value decomposition of $\boldsymbol{F_e}$ into $\boldsymbol{U}\boldsymbol{\Sigma}\boldsymbol{V}^\top$, where $\boldsymbol{U}$ and $\boldsymbol{V}$ are $3D$ and $2D$ rotations resp., and $\boldsymbol{\Sigma}$ is a rectangular diagonal matrix. We extract a 2×2 diagonal matrix $\boldsymbol{S} = \mathrm{diag}(\lambda_1, \lambda_2)$ by removing the last row of $\boldsymbol{\Sigma}$. The plastic deformation gradient $\boldsymbol{F_p}$ is updated by

$$\boldsymbol{F_p} \leftarrow \boldsymbol{V}(\det(\boldsymbol{S})^{-\frac{1}{2}}\boldsymbol{S})^\gamma \boldsymbol{V}^\top \;\; \boldsymbol{F_p}, \tag{6}$$

where the exponent γ indicates how much $\boldsymbol{F_p}$ is changed. To see that it reduces the strain, we can examine the corresponding update to $\boldsymbol{F_e}$,

$$\boldsymbol{F_e} \leftarrow \boldsymbol{F}\boldsymbol{F_p}^{-1} = \det(\boldsymbol{S})^{\frac{\gamma}{2}}\, \boldsymbol{U}\mathrm{diag}(\lambda_1^{1-\gamma}, \lambda_2^{1-\gamma})\boldsymbol{V}^\top. \tag{7}$$

The factor $\det(\boldsymbol{S})^{\frac{\gamma}{2}}$ insures that the plastic deformation does not modify the area, but it is close to 1 to begin with, as the material is nearly incompressible and the change to the thickness is much smaller than the stretches inside the membrane. Thus, γ within the range of $[0, 1]$ can bring down Green's strain (Eq. (1)) to meet the requirement of $\sigma_v = \sigma_y$. In [36] and [34], γ is a function of time or simulation step for the dynamical simulation. In our quasi-static calculation, we need to plastically deform the material until the hardening of plastic sheet is complete. So we calculate the value of γ to get the final state of $\boldsymbol{F_p}$ in each step.

Once the total deformation gradient $\boldsymbol{F}$ is updated in the elasticity update, we use binary search of $\sigma_v - \sigma_y$ as a function of γ in Eq. (6). Note that with a fixed total deformation gradient $\boldsymbol{F}$, both σ_v and σ_y are functions of γ. Since γ can reduce σ_v by lowering the strain to nearly 0, and $\sigma_y > \sigma_0$, we can always find a solution with $[0, 1]$, as mentioned in [36].

4.1.3 External forces.

1) Gravity. An obvious external force to consider is the gravity, but its effect on the result is minimal due to its relatively small magnitude compared to internal stress. The original internal stress within the plastic sheet is due to the typical manufacturing procedure, extrusion [23]. Such internal stress is relieved during the initial heating process. Before the heating begins, the boundary of the plastic sheet is fixed by the sheet clip on the vacuum forming machine, which we set as hard constraint throughout the simulation. With the fixed boundary, the sheet first curls due to the internal stress at the early stage of heating (about 1-3 minutes on our device), and then becomes smooth again

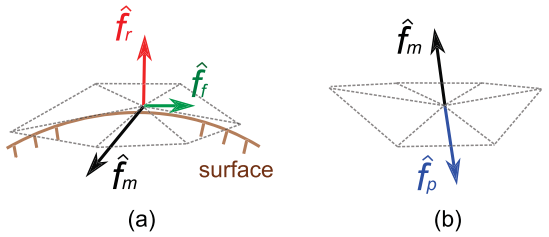

Fig. 5. Forces in the two stages of thermoforming. (a) Loading. The plastic sheet slips on the mold until the membrane force $\hat{f}_m$, repulsive force $\hat{f}_r$ and friction $\hat{f}_f$ reach equilibrium. (b) Vacuuming. The membrane force $\hat{f}_m$ and air pressure force $\hat{f}_p$ reaches equilibrium. Any vertices touching the mold serve as position constraints.

(around 3-5 minutes). Once the working temperature is reached, the sheet is ready for forming. Throughout the heating process, there is no visible drape in the sheet as the gravity is negligible compared to the internal stress. When the vacuuming begins, air pressure and contact forces become the dominating external forces. So we simply omit gravity throughout our simulation. For large sheets, it is also easy to introduce gravity through the sheet mass density times the constant gravitational acceleration.

2) Collision with 3D model. After the heating stage, we lower the plastic sheet until the sheet clip touches the model container. At this point, the plastic sheet may touch the 3D model and slide on the surface. Since the surface is static throughout the simulation, we pre-compute a signed distance field for the 3D model to perform fast collision detection on a regular grid (with $2\text{mm}\times2\text{mm}\times2\text{mm}$ cell-size) as in [42]. Our collision handling is modeled after [43], through repulsive forces determined by the distance to the surface. For each vertex of the sheet mesh, we check its distance to the 3D model surface by a trilinear interpolation of the distance field in the grid cell. If the distance value $d < h_0/2$, where h_0 is the original plastic sheet thickness (1mm in our experiments), we activate, for that vertex, a repulsive force expressed as

$$\hat{\boldsymbol{f}}_{\boldsymbol{r}} = \begin{cases} k_r(\frac{h_0}{2} - d)M\hat{\boldsymbol{n}}, & d < h_0/2 \\ \hat{\mathbf{0}}, & \text{otherwise} \end{cases}, \tag{8}$$

where M is one third of the one-ring area of the vertex, $\hat{\boldsymbol{n}}$ is the unit gradient of the signed distance field and k_r is a constant to control the repulsive force. We found this simple model adequate for achieving the desired accuracy in our experiments.

3) Friction with model surface. Friction, the tangential contact force, resists to slipping of the plastic sheet on the 3D model surface. We use the Coulomb's model to evaluate the friction $\hat{\boldsymbol{f}}_{\boldsymbol{f}}$. For each vertex of sheet, the maximum friction magnitude is $\mu\|\hat{\boldsymbol{f}}_{\boldsymbol{r}}\|$, where μ is the coefficient of friction between the contacting materials. We compare the maximum friction with the magnitude of $\boldsymbol{f_t}$, which is the tangential component of the sum of all other forces $\boldsymbol{f}$, calculated through a projection onto the plane perpendicular to $\hat{\boldsymbol{n}}$. Then the friction force (Fig. 5 (a)) $\hat{\boldsymbol{f}}_{\boldsymbol{f}}$ can be calculated as

$$\hat{\boldsymbol{f}}_{\boldsymbol{f}} = \begin{cases} -\boldsymbol{f_t}, & \|\boldsymbol{f_t}\| < \mu\|\hat{\boldsymbol{f}}_{\boldsymbol{r}}\| \\ -\mu\frac{\|\hat{\boldsymbol{f}}_{\boldsymbol{r}}\|}{\|\boldsymbol{f_t}\|}\boldsymbol{f_t}, & \text{otherwise} \end{cases}, \tag{9}$$

4) Atmosphere pressure. When the plastic sheet reaches the equilibrium state, we start the vacuum forming. At this stage, the air pressure forces the plastic sheet to press against the model surface and be attached to it firmly. We gradually increase the air pressure until the end of the procedure. In the simulation, we first calculate the air pressure force on each triangle, and then evenly distribute the force to its three vertices. The force on each triangle is calculated by

$$\boldsymbol{f_p} = -pA\hat{\boldsymbol{n}}, \tag{10}$$

where p is the current air pressure difference between the top and the bottom sides of the sheet, A is the area of the triangle and $\hat{\boldsymbol{n}}$ is the unit normal of the triangle. The sum of the distributed $\boldsymbol{f_p}$ from the one-ring of a vertex provides the air pressure force on the vertex $\hat{\boldsymbol{f}}_{\boldsymbol{p}}$ (Fig. 5 (b)). We assume a constant pressure difference p for all triangles, as often done in vacuum-based thermoforming simulations. This assumption also allows us to provide an efficient treatment of air pockets formed during the process (in Sec. 5). As soon as the air pressure brings any part of the plastic sheet into contact with the model surface, it will be held there firmly. So we assume no slipping in the vacuum forming stage. It means that once we detect the distance value of a vertex from the surface to satisfy $d < h_0/2$, we constrain the vertex position to be the point where $d = h_0/2$ along the line segment between the current position and the previous position, by iterative search. We use the original thickness h_0 in this calculation, since the thickness change of the sheet can be safely ignored.

4.2 Implementation of Numerical Simulation

We use finite element method to simulate the plastic sheet. In our discretization of the plastic sheet, its fixed boundary is a rectangle that fits into the sheet clip. A triangular tessellation of the sheet was generated using the mesh library: Triangle [44], with a lower bound of 30° for interior angle and an upper bound of $2mm^2$ for triangle area. The simulation starts from hanging the plastic sheet above the model (Fig. 1 (a)). We first simulate the collision of the sheet with the model during when loaded into the working position, and then activate the pressure difference for vacuuming (Fig. 1 (b)). Since the whole procedure is fast, we can ignore the effects of the change in temperature.

We formulate the simulation as a backward Euler update. In each simulation step, we first update the vertex positions based on balancing the forces in the quasi-step simulation. The internal stress is calculated based on the elastic deformation gradient $\boldsymbol{F}\boldsymbol{F}_{\boldsymbol{p}}^{-1}$, where $\boldsymbol{F}$ is a function of the vertex positions, and $\boldsymbol{F}_{\boldsymbol{p}}^{-1}$ is the plastic deformation gradient in the previous step. The other forces, including the air pressure, the repulsive force, and the friction, are all functions of the vertex positions through their dependence on the normal, the area, and the distance to the model surface. Since the gradients of all the forces can be easily derived, we solve the nonlinear force balance equations by Newton's method, with 50 Newton iterations per simulation step. For each iteration, the linear system was solved by a Conjugate Gradient solver.

With the updated vertex position, we perform the plastic deformation update. We first detect the triangles satisfying

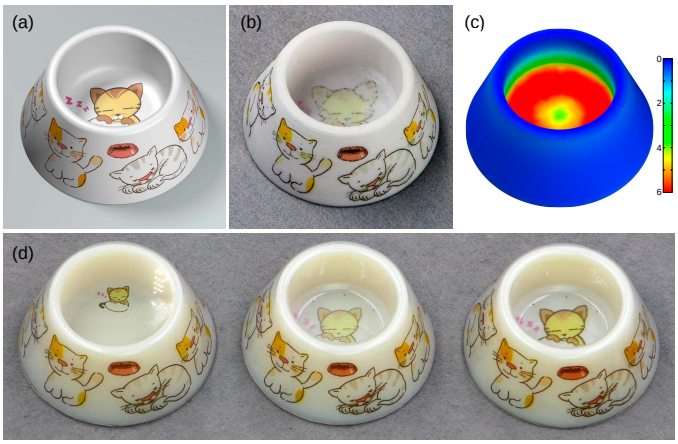

Fig. 6. We decorate a cat bowl with both outside and inside surfaces. (a) The desired texture. (b) The result of computational hydrographics, the texture at the bottom has become highly distorted due to large stretch. (c) The area extension rate of the plastic sheet when attached to the model surface. (d) Our result, we put 3 models side by side to compare color deviation. (left) The forming result without setting vacuum holes, the plastic sheet cannot attach to the inner surface due to trapped air. The small cat pattern in the middle reveals the size and pigment density of the pattern before stretch (without color adjustment). (middle) With vacuum holes but without color adjustment, the color at the bottom has become lighter very obviously due to large stretch. (right) Color adjustment is introduced, and the color deviation has been reduced.

the von Mises criteria $\sigma_v > \sigma_y$. For each of these triangles, we use binary search to update $\boldsymbol{F_p}$ so that $\sigma_v = \sigma_y$. The new plastic deformation gradient is used in the next simulation step.

4.3 Pattern Computation

When the simulated plastic sheet is fully attached to the 3D model surface, we have established a mapping between the plastic sheet and the model surface. This mapping induces a mapping between the pattern to print on the sheet, and the desired appearance on the 3D model surface. The pattern can thus be calculated in a straightforward procedure similar to the one used in [1], as we detail below.

The pattern image to be printed on the plastic sheet can be seen as a texture of the sheet mesh. For each pixel of the pattern image, we can locate the triangle of the sheet mesh based on its position $\boldsymbol{x}$, and evaluate barycentric weights of the pixel within the triangle. Since the mesh connectivity of the plastic sheet does not change during the simulation, the final location $\boldsymbol{x'}$ of the pattern pixel on the deformed sheet can be found by weighted average of the vertex positions of the same triangle after the simulation, weighted by the same barycentric weights. Since $\boldsymbol{x'}$ is on the flat triangle of the final sheet mesh, it may deviate slightly from the model surface mesh. So we project it to the nearest point $\tilde{\boldsymbol{x}}$ on the model surface. The color of $\tilde{\boldsymbol{x}}$ can be retrieved from the texture of the 3D model and assigned to the pixel at $\boldsymbol{x}$ in the pattern image. The final pattern is assembled by going through all pixels.

We can further improve the quality of the resulting appearance by compensating for the stretching of the sheet. The non-uniform stretching in the sheet induces variations in local density of pigment, as shown in Fig. 6. Our method for color adjustment is similar to [2]. For each pixel at $\boldsymbol{x}$, we use the triangle that contains this point to calculate the triangle areas $\boldsymbol{A_x}$ and $\boldsymbol{A'_x}$ before and after simulation. The ratio of pigment density is inversely proportional to the the area ratio, due to mass preservation. Since the target surface pigment density at $\tilde{\boldsymbol{x}}$ can be measured in CMYK (Cyan-Magenta-Yellow-Black) color space and denoted as $\boldsymbol{c_{\tilde{x}}}$, we can set the pigment density to be printed on the sheet at $\boldsymbol{x}$ to $(\boldsymbol{A'_x}/\boldsymbol{A_x})\boldsymbol{c_{\tilde{x}}}$. For severely stretched regions, the density is out of range for a single pass printing, we can print multiple times to reach the desired pigment density. Such a procedure can be directly carried out on regular printers, such as the profiled CMYK LaserJet color printer we use. The effects of appearance of color compensation can be seen in Fig. 6. This adjustment in pigment density does not require a re-run of the simulation, since the pigment density has virtually no effect on the stretching of typical thermoforming plastic sheets, as those sheets have large Young's modulus, unlike the media used in hydrographics-based color transfer in [1].

5 Model Adaptation for Thermoforming

During the vacuum forming process of our virtual simulation, we assume that for all points on the plastic sheet that have not yet reached the model surface, the pressure differences between the two sides of the sheet are the same. However, this assumption is only approximately true when all spaces between the plastic sheet and the model are connected to the vacuum pump. In practice, if the 3D model surface contains concave regions, for example, a large dent, it is highly likely that the rim of the dent will be covered by the plastic sheet during the process, leaving the air trapped inside the dent, as shown in Fig. 7. To prevent this from happening, we need to detect potential air pockets during the virtual simulation and compute a layout of vacuum holes (also called vent holes) at the bottom of these regions. Air can then be sucked out through these channels, allowing the plastic sheet to adhere to the model surface tightly.

5.1 Air Pocket Detection

Air pockets are formed between the triangle mesh of the sheet and the target surface, but we can actually detect their formation directly on the sheet mesh during the simulation. In any simulation step in the vacuum forming stage, if a vertex of the sheet touches the model surface, it will be attached there permanently. When both vertices of an edge are

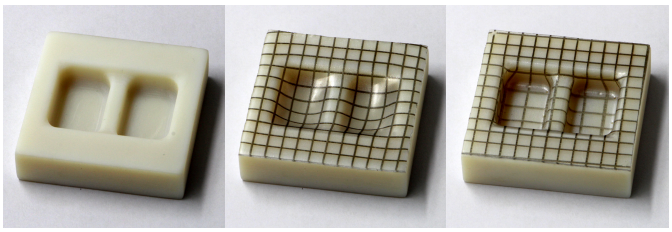

(a) (b) (c)

Fig. 7. We compare the forming results of a concave model with and without vacuum holes: **(a)** the mold used for thermoforming, **(b)** if no vacuum holes are set on the mold, air will be trapped in concave regions, and **(c)** after vacuum holes are drilled or preset before printing the mold, air will be exhausted through these holes and the plastic sheet will adhere tightly to the mold surface.

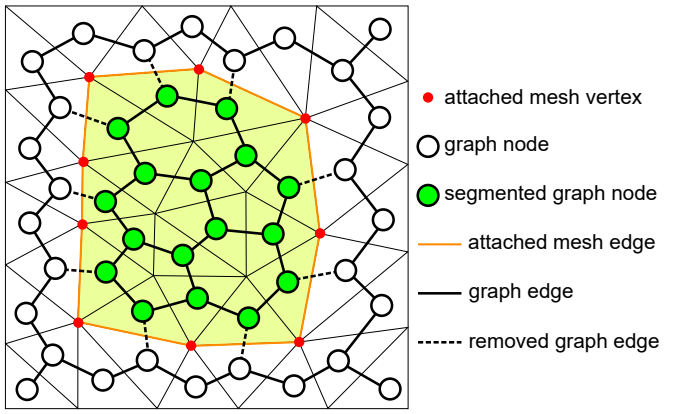

Fig. 8. To detect air pockets, we create a weak dual graph for the triangle mesh of the plastic sheet. During the simulation, mesh vertices will attach to the model surface. A mesh edge becomes an attached edge when both of its vertices are attached to the model surface, the corresponding graph edge will be removed. If a connected component surrounded by attached edges is detected, the corresponding sheet mesh faces (shown as the light yellow region) will form an air pocket with the region enclosed by the same loop on the model surface.

attached to the model surface, we call it an attached edge. An attached edge prevents air from flowing under it. When such attached edges form a loop around an unattached region on the sheet mesh, air will be trapped in the cavity formed by this region of the sheet and the region of the model surface bounded by the same loop, assuming that the model surface has disk-like topology. Thus, the formation of an air pocket can be detected by attached edge loops.

The exact procedure to detect air pockets can be formulated on the weak dual graph $\boldsymbol{G} = (\boldsymbol{V}, \boldsymbol{E})$ of the sheet mesh, as shown in Fig. 8. Each graph node $\boldsymbol{V_i} \in \boldsymbol{V}$ represents a mesh triangle and each graph edge $\boldsymbol{E_i} \in \boldsymbol{E}$ corresponds the mesh edge connecting two adjacent triangles. If an edge becomes attached, the corresponding graph edge $\boldsymbol{E_i}$ will be removed from $\boldsymbol{E}$. In each simulation step, the graph $\boldsymbol{G}$ is updated and we detect connected components $\boldsymbol{C} \subset \boldsymbol{G}$ every frame. If one new connected component $\boldsymbol{C_i}$ is detected and the corresponding triangle mesh region $\boldsymbol{R_i}$ contains unattached vertices and is surrounded by attached edges, this region is marked as covering a new air pocket. The space beneath that region can actually still be connected to the vacuum pump or other air pockets, if the 3D model contains tunnels. However, while it is possible to examine the corresponding regions on the model surface to verify the formation of an air pocket, we skip such additional operations since our prototype thermoforming system only handles genus-0 surfaces.

5.2 Air Pocket Forest

In addition to detecting air pockets, we also need to track the evolution of the air pockets in the simulation, so as to determine the number and locations of the vacuum holes to eliminate them effectively. For that purpose, we introduce the concept of air pocket forest, in which each root denotes an air pocket formed by an attached edge separating it from the outside region connected to the vacuum pump, each leaf denotes an air pocket disappearing when the last unattached vertex in the region becomes attached to the

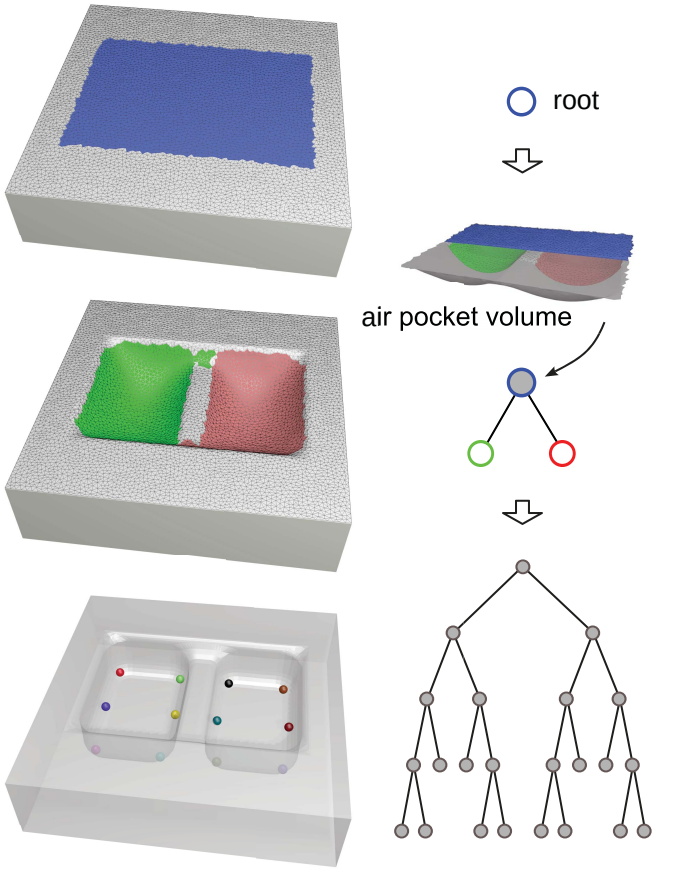

Fig. 9. Formation of an air pocket forest. Root nodes are created when air pockets are created by loops disconnecting a region from the mesh boundary, internal nodes are created when existing air pockets split into smaller air pockets by attached edges, and leaf nodes are those disappearing without being split.

model surface, and each internal node denotes an air pocket splitting into two air pockets by a newly attached edge, as shown in Fig. 9. Roughly speaking, the vacuum holes should be placed at the location of the leaf nodes to exhaust the cavity air. However, there are often numerous leaf nodes with the naive detection procedure. So we describe below how to filter out the unnecessary ones.

First, we make the observation that if we reverse the simulation time, we can see the process as gradually adding nodes and edges to the dual graph and tracking the connected components formed and merged as in the upside down air pocket forest. This is directly linked to theory of persistent homology in computational topology [37], which provides readily available tools for eliminating low persistence (i.e., short-lived) air pockets, generated due to small bumps on the 3D model surface, or discretization errors of the plastic sheet. Such tiny air pockets exist in the numerical simulation, but can hardly be observed in practice due to the trapped air leaking through the small undulation in the actual surface or the porosity of the material. In the following, we describe the tracking procedure using the air pocket forest. Its construction can be seen as based on the concept of the persistent 0-th homology, which tracks the life cycles of the connected components of unattached parts of the thin sheet. However, there is one main modification:

we do not use the appearing time, disappearing time or split time to measure the persistence, but rely on a more relevant physical quantity for the vacuuming procedure, the volume of cavity air.

During the virtual simulation, an air pocket $\boldsymbol{P_i}$ appears when the connected component $\boldsymbol{C_i}$ is detected at time $\boldsymbol{t_1}$, and disappears when all vertices in region $\boldsymbol{R_i}$ are attached to the model surface at $\boldsymbol{t_2}$. The shape of $\boldsymbol{R_i}$ is recorded at these two time steps and denoted by $\boldsymbol{R_i^{t_1}}$ and $\boldsymbol{R_i^{t_2}}$. The space enclosed by $\boldsymbol{R_i^{t_1}}$ and $\boldsymbol{R_i^{t_2}}$ is the air pocket $\boldsymbol{P_i}$. Thus the volume of $\boldsymbol{P_i}$ can be calculated through the closed triangle mesh formed by $\boldsymbol{R_i^{t_1}}$ and reversed $\boldsymbol{R_i^{t_2}}$.

When existing big connected component $\boldsymbol{C_i}$ splits into multiple smaller connected components, the associated air pocket $\boldsymbol{P_i}$ splits into several smaller air pockets at a certain time step, forming an internal node in the air pocket forest. Such a node indicates that the vacuum holes in either child regions can exhaust air in parent region. So we recursively merge air pockets whose volume is less than a threshold into their parents by trimming the branch and adding the volume to the branching node. We keep merging air pockets until the volume of all remaining air pockets in the forest are above the threshold to set vacuum holes. In our experiment, the volume threshold is set to 1mm^3. Note that entire tree can be removed if the total volume is still below the threshold.

5.3 Vacuum Holes

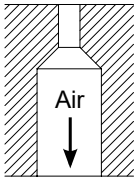

Once the air pocket forest is processed, we start placing vacuum holes. The shape of a typical vacuum hole is shown on the right. The opening of the hole is small to avoid leaving visible marks on the plastic sheet, while the diameter increases below the model surface to increase air flow. The optimal opening diameter of a hole depends on the type and thickness of the plastic sheet [23]. In our experiment, we choose the diameter at the opening to be 1mm and diameter at the enlarged air channel to be 3mm, which starts 3mm below the model surface. The flow capacity of this hole is about $100\text{cm}^3/\text{s}$ on our device.

For each leaf node in the air pocket forest, we record the last vertex to be attached to the model surface. The corresponding attaching point on the 3D model is the location where the vacuum hole is set. In this way, air in all pockets can be exhausted from these vacuum holes. However, the amount air flow through each vacuum hole is limited in unit time. So when the space the model and sheet is extremely large, the number of vacuum holes to effectively vent the air should also be calculated. In our experiment, since the models are sufficiently small, we found one vacuum hole per leaf node is adequate. The extension to multi-hole calculation should be easy since we have calculated the volume of each air pockets in the forest.

For each vacuum hole, we direct the narrow channel toward the opening along the surface normal at the location of the hole. The wider part of the channel is always along vertical direction. For complex models, to prevent damage to intricate details of the model surface, it is possible to use a simple user interface to allow optional manual adjustment to edit the layout of vacuum holes. We leave this as a direction for future work.

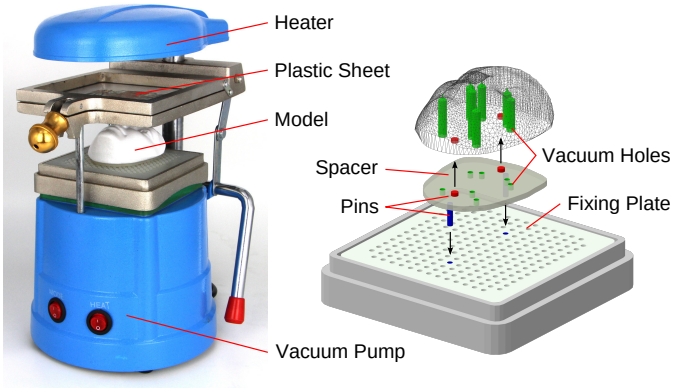

Fig. 10. The setup of thermoforming. (left) The device we use with sheet and model fixed on the machine. (right) How the model is fixed to the model container.

6 Prototype Surface Coloring System

To build an easily accessible physical implementation of our thermoforming coloring framework, we use a low-end small scale vacuum forming machine, which is commonly seen in dental clinics for fitting plastic braces. The system configuration is shown in the left of Fig. 10. The size of its working area is $11\text{cm} \times 11\text{cm}$. It is designed to hold plastic sheet of size $13\text{cm} \times 13\text{cm}$ and thickness $1 \sim 2\text{mm}$ by the sheet clip, which can be moved up and down vertically by turning a handle. In our experiments, we use transparent polyethylene (PE) sheets of 1mm thickness provided by the manufacturer of the thermoforming machine. In industrial applications, thermoforming materials may include a variety of plastics, such as acrylonitrile butadiene styrene (ABS), polypropylene (PP), and polystyrene (PS). Nevertheless, similar simulations can still be performed with adjusted parameters, since the behaviors of these materials are similar in the forming process.

In order to obtain the desired texture on the 3D model, the system must align the printed pattern to the plastic sheet, and align the sheet to the 3D printed model. Otherwise, the accuracy we achieve in the virtual simulation will be lost in the physical implementation. Thus, we designed some simple mechanisms to ensure that the pattern on the plastic sheet and the 3D model to be in the same relative position and orientation each time we operate the machine. We elaborate on these procedures in each of the physical printing stages in the following subsections.

6.1 Sheet Printing

Our virtual simulation of the plastic sheet already takes into account the alignment the printed pattern to the machine, as the boundary of the sheet mesh is fixed to a square with the size of the working region of the machine. Since the color printer we use is profiled, the printed square with the simulated color pattern can be accurately aligned with the inner boundary of the sheet clip when we clamp the sheet to the clip. We only need to make sure that the two squares are aligned.

We use decal technique to achieve the alignment of the printed pattern on the plastic sheet. The pattern is first printed on a standard A4 sized decal film using an HP Color LaserJet CP3525dn. As the decal film is a very thin piece of plastic, it is attached to strong supporting paper when printing. Then we trim the decal film to the size of the plastic sheet, detach it from the supporting paper and attach it to the plastic sheet surface. The plastic sheet with printed pattern is well-aligned and ready for use.

Since we use transparent plastic sheets, it is fine to attach the decal film to either side of the plastic sheet. In our experiments, we attach the decal film between the plastic sheet and the model, so that the plastic sheet will serve as a cover to protect the texture. It also gives the 3D model a smooth and glossy appearance. Other appearances are also possible, with, e.g., matte coating post-processing.

With decal film attached, the plastic sheet becomes less stretchable, so the physical parameters of the plastic sheet in virtual simulation are actually estimates that describe the combination of the plastic sheet and the attached decal film.

It would have been more convenient and accurate to print the pattern on the plastic sheet directly using a UV flatbed printer. However, since the plastic sheet will be heated and stretched during the thermoforming process, traditional UV ink may suffer from color change when heated and even cracking when stretched. So special inks for thermoforming have to be used [27] if a UV flatbed printer is used. In contrast, the pigment printed using the LaserJet is based on halftoning instead of a continuous layer of ink, so our decal-based procedure does not suffer from this problem.

6.2 Model Printing

In order to produce results in agreement to the simulation, the positions of 3D models are precisely fixed to the machine using pins, as shown in the right of Fig. 10. At the bottom layer, we print a fixing plate, which can fit into the mold container of the machine tightly. The fixing plate contains a regular grid of holes so that it can be used with various models. These holes serve as pin holes as well as vacuum holes. On top of the fixing plate, we put a supplementary spacer, printed for each model, which is essentially an extrusion from the bottom of the model. Vacuum holes on the model extend into the spacer. The spacer also contains four pins, two downward pins are used to locate the spacer to the fixing plate, the other two upward pins are used to fix the model, which will be placed on top of the spacer. In this way, the model is easily fixed through the spacer and the fixing plate to the machine. The reason to add the spacer is for easy trimming of the plastic sheet after thermoforming.

We use a Stratasys Eden260v 3D printer to print the models in our experiments with the VeroWhitePlus material. This 3D printer can achieve high precision and the printed model surface can be highly smooth after polishing. If the working surface of the model is a height field, the formed plastic sheet can be unloaded from it very easily. So such smooth models can serve as molds for mass production of the same colored surface sheets. It is also possible to use less costly Fused Deposition Modeling (FDM) 3D printers, but the unloading is not as simple because the hot plastic sheet adheres tightly to the rough printed surface. For these models, we just perform thermoforming once, and leave the plastic sheet on the model surface to serve both as texture and as a polishing layer.

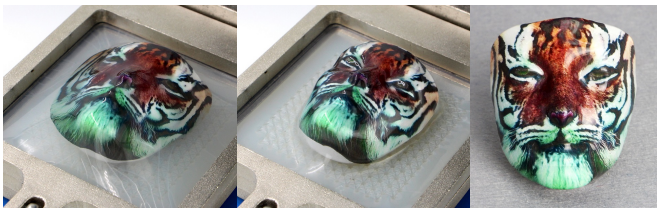

(a) (b) (c)

Fig. 11. The forming process: **(a)** The plastic sheet is heated to working temperature and loaded to the forming position, **(b)** The atmospheric pressure pushes the plastic sheet onto the model surface, **(c)** The plastic sheet hardens again as it cools down. After the boundary is trimmed, the model is decorated with desired color texture.

6.3 Vacuum Forming

With the plastic sheet clamped on the sheet clip and the model loaded on the model container, we start thermoforming. First, we remove the model container from the machine and lower the sheet clip so that the plastic sheet can be heated evenly. Then we start the heater to soften the plastic sheet. The temperature of the plastic sheet affects its physical property, so we heat the plastic sheet by exactly the same amount of time (5 minutes in our experiments) before forming to match with the parameters used in the simulation.

After heating is complete, we immediately raise the sheet clip, load the model container to the machine and lower the plastic sheet again. The plastic sheet begins to stretch upon touching the model surface, as shown in Fig. 11(a). When the sheet clip is lowered to the working position, a sealed space is formed under the sheet. As we start the vacuuming pump, the plastic sheet is quickly stretched under air pressure and pressed against the model surface. The pattern is stretched along with the sheet and adhered to the surface, as shown in Fig. 11(b). After the plastic sheet cools down, we turn off the vacuuming pump. Once we trim the plastic sheet along the bottom of the model, the production of a model with color texture is complete, see Fig. 11(c). We refer to the supplementary video for the entire thermoforming process.

7 Experimental Results

Our simulation system was run on an Intel i7-4930K 3.4GHz CPU and 64G RAM. In the simulation, we use an input mesh of the plastic sheet that contains 5148 vertices and 10058 triangles – the simulation result does not change noticeably with higher-resolution meshes. Our current code is not optimized and uses only a single CPU thread. Nevertheless, the computation time of all our experiments finished within one minute, including simulation and realtime rendering. We believe the performance can be further improved, by employing multi-thread programming or even GPU computing.

In the simulation of sheet deformation, there are four main physical parameters for the material of the plastic

sheet (attached with decal film): Young's modulus, Poisson's ratio, initial yield stress and hardening coefficient. The value of the Young's modulus ($Y = 1$MPa) at forming temperature is provided by the plastic sheet manufacture. The Poisson's ratio of polymers when passed yield point is about 0.5 as mentioned in [39], which means that the material becomes incompressible when undergoing plastic deformation. Since we have a relatively low yield stress and plastic deformation starts at a very early stage, we simply treat the Poisson's ratio ($\nu = 0.5$) to be constant through the simulation. The value of initial yield stress ($\sigma_0 = 220$Pa) and hardening coefficient ($K = 1000$Pa) are determined by experiment. We use a plastic sheet printed with grid pattern to perform a standard thermoforming procedure with a truncated cone (Sec. 7.1) as mold. Then, we perform a series of virtual simulations with different σ_0 and K values and choose the values that yield the best matching results to the real experiment. We perform a single physical experiment, and multiple simulations with σ_0 and K chosen from a 20×20 combination of values. With the total running time of about one hour, we can easily refine the parameters with another round of 400 simulations based on the first round estimates if necessary. It is also possible to scan the result of real experiment and select the best matching automatically, as described in [28].

The stiffness constant k_r to control repulsive force in collision (Sec. 4.1.3) was manually set at $k_r = 5 \times 10^8 N/m^3$. This coefficient needs to be sufficiently large to prevent any visible penetration in our experiments. The coefficient of friction μ depends both on the plastic sheet and the material for 3D printing. For the VeroWhitePlus material used by the Stratasys Eden260v 3D printer, $\mu = 0.8$ provides a reasonable approximation in simulation. For models with very rough surfaces, such as the ones printed using FDM 3D printer, there is almost no visible slipping. In this case, we can further simplify the simulation by fixing the vertices as soon as they touch the surface of the 3D model.

7.1 Accuracy

We validate the accuracy of our method using a truncated cone with a cross-line texture, as shown in Fig. 12(a). The height of the truncated cone is 3cm, with a top radius of 1cm and a bottom radius of 2cm. Seven blue circles are evenly spaced on the lateral conic surface with the top and bottom circles snapped to the circular perimeters of the top and the base respectively.

We ran the virtual simulation for the truncated cone, calculated the pre-distorted texture and attached the texture to the cone using thermoforming. The result is shown in Fig. 12(b). We can see that the blue circles on the resulting model appear at the same position of the texture model. The error in cross-line alignment is lower than 1mm.

7.2 Comparison with hydrographics

We compare our result with computational hydrographic printing [1], as shown in Fig. 6. The plastic sheet attached to the bottom of the cat bowl is stretched to over 6 times of the original area. In hydrographics, such a big stretch will break the viscous film, resulting in a highly distorted transferred image, as shown in Fig. 6(b). The stretching of plastic sheet

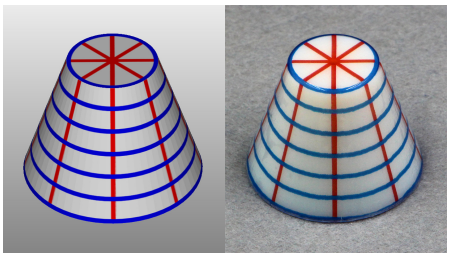

(a) (b)

Fig. 12. Accuracy validation on a truncated cone with cross-line texture. (a) the desired texture, (b) the resulting model. Our system can decorate the model surface with desired texture with better than 1mm accuracy.

is more uniform than viscous sheet with large strain, so the final texture is well preserved. As mentioned in Sec. 4.3, the drastic increase in sheet area leads to decrease in pigment density, so color adjustment when calculating the image can alleviate the color distortion in over stretched areas, as shown in Fig. 6(d). Unlike hydrographic printing, which transfers pigment only, thermoforming uses the plastic sheet as a carrier, so an extra layer of plastic would cover the original material (e.g., metal, wood or porcelain), which may or may not be desirable for the application.

7.3 Gallery of results

Fig. 13 shows more results we have produced using thermoforming. The relief of a female actor's head was generated from a single image using the method proposed in [45]. The model is a height field aligned with each pixel. We printed the relief and decorated it with the correct pixels. The turtle model has several extruded parts, including its legs, tail and head, we can decorate them with the proper texture in a single thermoforming process. The sport car is not a height field, so we have to decorate the entire surface except the bottom. The plastic sheet wraps around the whole car body and transfers the color as designed.

Note that except the turtle, the other models need vacuum holes to avoid air pockets. Specifically, 7 holes are created for the mask model (Fig. 11), 12 for the relief, 6 for the car, and 8 for the cat bowl.

8 Conclusion

We present a thermoforming surface color printing technique, with virtual simulation based texture warping and automatic vacuum hole layout generation. We also provide the procedures to prepare a prototype hardware framework for 3D printed surface coloring, with off-the-shelf components. Our coloring process virtually eliminates all visible air pockets even in highly concave regions, owing to the air pocket forest structure, which keeps track of the evolution of air pockets and provide optimal locations for vent holes. Our surface color transfer also handles stretching better than the state-of-the-art hydrographics approach as the plastic sheets extend more uniformly under stress.

Our current design has a number of limitations. It can only handle genus-0 surfaces, and the accuracy is the best for height field. The simulation does not contain self-collision detection, so it would not be able to handle the case

Fig. 13. Colored 3D prints produced using our method. The upper left image next to each model is the rendering result and the lower left image shows the model produced by 3D printing before coloring.

when the sheet wraps around handle-like structures and collides into itself. The openings of the vacuum holes may be undesirable if the interior of the 3D models are not to be modified. For future work, we wish to explore the extension to high genus objects, possible multi-pass thermoforming, better model orientation to wrap more regions including the bottom part, dynamical instead of quasi-static simulation to further improve the accuracy, and other types of reflectance material to produce diffuse, anisotropic, or even user specified BRDFs.

Acknowledgments

This work is supported by the NSF of China (No. 61272305), the National Program for Special Support of Eminent Professionals of China, and Lenovo's Program for Young Scientists. Y. Tong wishes to thank the support of the State Key Lab of CAD&CG for his stay at Zhejiang University, during which he participated in this work. Kun Zhou is the corresponding author of this paper.

References

[1] Y. Zhang, C. Yin, C. Zheng, and K. Zhou, "Computational hydrographic printing," *ACM Trans. Graph.*, vol. 34, no. 4, pp. 131:1–131:11, Jul. 2015.
[2] D. Panozzo, O. Diamanti, S. Paris, M. Tarini, E. Sorkine, and O. Sorkine-Hornung, "Texture mapping real-world objects with hydrographics," in *Comput. Graph. Forum*, vol. 34, no. 5. Wiley Online Library, 2015, pp. 65–75.
[3] O. Stava, J. Vanek, B. Benes, N. Carr, and R. Měch, "Stress relief: Improving structural strength of 3d printable objects," *ACM Trans. Graph.*, vol. 31, no. 4, p. 48, 2012.
[4] M. Bächer, B. Bickel, D. L. James, and H. Pfister, "Fabricating articulated characters from skinned meshes," *ACM Trans. Graph.*, vol. 31, no. 4, p. 47, 2012.
[5] J. Calì, D. A. Calian, C. Amati, R. Kleinberger, A. Steed, J. Kautz, and T. Weyrich, "3d-printing of non-assembly, articulated models," *ACM Trans. Graph.*, vol. 31, no. 6, p. 130, 2012.
[6] S. Coros, B. Thomaszewski, G. Noris, S. Sueda, M. Forberg, R. W. Sumner, W. Matusik, and B. Bickel, "Computational design of mechanical characters," *ACM Trans. Graph.*, vol. 32, 2013.
[7] D. Ceylan, W. Li, N. J. Mitra, M. Agrawala, and M. Pauly, "Designing and fabricating mechanical automata from mocap sequences," *ACM Trans. Graph.*, vol. 32, no. 6, p. 186, 2013.
[8] R. Prévost, E. Whiting, S. Lefebvre, and O. Sorkine-Hornung, "Make it stand: balancing shapes for 3d fabrication," *ACM Trans. Graph.*, vol. 32, no. 4, p. 81, 2013.
[9] B. Thomaszewski, S. Coros, D. Gauge, V. Megaro, E. Grinspun, and M. Gross, "Computational design of linkage-based characters," *ACM Trans. Graph.*, vol. 33, no. 4, pp. 64:1–64:9, Jul. 2014.
[10] B. Bickel, M. Bächer, M. A. Otaduy, W. Matusik, H. Pfister, and M. Gross, "Capture and modeling of non-linear heterogeneous soft tissue," *ACM Trans. Graph.*, vol. 28, no. 3, pp. 89:1–89:9, Jul. 2009.
[11] M. Skouras, B. Thomaszewski, S. Coros, B. Bickel, and M. Gross, "Computational design of actuated deformable characters," *ACM Trans. Graph.*, vol. 32, no. 4, p. 82, 2013.
[12] J. Panetta, Q. Zhou, L. Malomo, N. Pietroni, P. Cignoni, and D. Zorin, "Elastic textures for additive fabrication," *ACM Trans. Graph.*, vol. 34, no. 4, p. 135, 2015.
[13] C. Schumacher, B. Bickel, J. Rys, S. Marschner, C. Daraio, and M. Gross, "Microstructures to control elasticity in 3d printing," *ACM Trans. on Graph.*, vol. 34, no. 4, p. 136, 2015.
[14] T. Weyrich, P. Peers, W. Matusik, and S. Rusinkiewicz, "Fabricating microgeometry for custom surface reflectance," *ACM Trans. Graph.*, vol. 28, no. 3, p. 32, 2009.
[15] W. Matusik, B. Ajdin, J. Gu, J. Lawrence, H. P. A. Lensch, F. Pellacini, and S. Rusinkiewicz, "Printing spatially-varying reflectance," *ACM Trans. Graph.*, vol. 28, no. 5, p. 128, 2009.
[16] Y. Lan, Y. Dong, F. Pellacini, and X. Tong, "Bi-scale appearance fabrication," *ACM Trans. Graph.*, vol. 32, no. 4, p. 145, 2013.
[17] Y. Dong, J. Wang, F. Pellacini, X. Tong, and B. Guo, "Fabricating spatially-varying subsurface scattering," *ACM Trans. Graph.*, vol. 29, no. 3, p. 62, 2010.
[18] M. Hašan, M. Fuchs, W. Matusik, H. Pfister, and S. Rusinkiewicz, "Physical reproduction of materials with specified subsurface scattering," *ACM Trans. Graph.*, vol. 29, no. 3, p. 61, 2010.
[19] T. Malzbender, R. Samadani, S. Scher, A. Crume, D. Dunn, and J. Davis, "Printing reflectance functions," *ACM Trans. Graph.*, vol. 31, no. 3, p. 20, 2012.
[20] M. Schlesinger and M. Paunovic, *Modern electroplating*. John Wiley & Sons, 2011, vol. 55.
[21] L. Darty, *The art of enameling: techniques, projects, inspiration*. Lark Books, 2004.
[22] R. Hopper, *Making Marks: Discovering the Ceramic Surface*. Krause Publications Craft, 2004.
[23] P. Klein, "Fundamentals of plastics thermoforming," *Synthesis Lectures on Materials Engineering*, vol. 1, no. 1, pp. 1–97, 2009.
[24] S. Junk, J. Sämann-Sun, and M. Niederhofer, "Application of 3d printing for the rapid tooling of thermoforming moulds," in *Proceedings of the 36th International MATADOR Conference*. Springer, 2010, pp. 369–372.
[25] J. Mellor, M. Oder, J. Starr, and J. Meador, "An image-based three-dimensional digitizer for pre-decorating thermoformed parts." in *BMVC*. Citeseer, 2003, pp. 1–10.
[26] M. Pollack and A. Jollett, *Reproducible three dimensional vacuum forming technique*. US Patent 8406508B2, 2013.
[27] S. Craig, "Direct digital uv imaging for deep draw thermoforming," *Thermoforming Quarterly*, vol. 32, pp. 24–26, 2013.
[28] C. Schüller, D. Panozzo, A. Grundhöfer, H. Zimmer, E. Sorkine, and O. Sorkine-Hornung, "Computational thermoforming," *ACM Transactions on Graphics (Proceedings of ACM SIGGRAPH)*, vol. 35, no. 4, 2016.
[29] Accuform, 2015, http://www.t-sim.com/.
[30] H. Nied, C. Taylor, and H. Delorenzi, "Three-dimensional finite element simulation of thermoforming," *Polymer Engineering & Science*, vol. 30, no. 20, pp. 1314–1322, 1990.
[31] G. J. Nam, J. W. Lee, and K. H. Ahn, "Three-dimensional simulation of thermoforming process and its comparison with experiments," *Polymer Engineering & Science*, vol. 40, no. 10, pp. 2232–2240, 2000.
[32] M. Warby, J. Whiteman, W.-G. Jiang, P. Warwick, and T. Wright, "Finite element simulation of thermoforming processes for poly-

mer sheets," *Mathematics and computers in simulation*, vol. 61, no. 3, pp. 209–218, 2003.
[33] J. Dees, *FEA Simulations of Thermoforming–Using Hyperelastic Material Properties*. Engineering simulations LLC, scientific article, 2009.
[34] A. W. Bargteil, C. Wojtan, J. K. Hodgins, and G. Turk, "A finite element method for animating large viscoplastic flow," *ACM Trans. Graph.*, vol. 26, no. 3, Jul. 2007.
[35] C. Wojtan and G. Turk, "Fast viscoelastic behavior with thin features," *ACM Trans. Graph.*, vol. 27, no. 3, pp. 47:1–47:8, Aug. 2008.
[36] T. Pfaff, R. Narain, J. M. de Joya, and J. F. O'Brien, "Adaptive tearing and cracking of thin sheets," *ACM Trans. Graph.*, vol. 33, no. 4, pp. 110:1–110:9, Jul. 2014.
[37] H. Edelsbrunner and J. Harer, *Computational topology: an introduction*. American Mathematical Soc., 2010.
[38] C. Park, H. Huh, J. Kim, and C. Ahn, "Determination of true stress–true strain curves of polymers at various strain rates using force equilibrium grid method," *Journal of Composite Materials*, vol. 46, no. 17, pp. 2065–2077, 2012.
[39] R. Park, M. Priestley, and W. Walpole, "The seismic performance of steel encased reinforced concrete bridge piles," 1982.
[40] M. A. Meyers and K. K. Chawla, *Mechanical behavior of materials*. Cambridge university press Cambridge, 2009, vol. 2.
[41] Y. Yue, B. Smith, C. Batty, C. Zheng, and E. Grinspun, "Continuum foam: A material point method for shear-dependent flows," *ACM Trans. Graph.*, vol. 34, no. 5, pp. 160:1–160:20, Nov. 2015.
[42] A. Fuhrmann, G. Sobotka, and C. Groß, "Distance fields for rapid collision detection in physically based modeling," in *Proceedings of GraphiCon 2003*, 2003, pp. 58–65.
[43] R. Bridson, R. Fedkiw, and J. Anderson, "Robust treatment of collisions, contact and friction for cloth animation," in *ACM Trans. Graph.*, vol. 21, no. 3. ACM, 2002, pp. 594–603.
[44] J. R. Shewchuk, "Triangle: Engineering a 2d quality mesh generator and delaunay triangulator," in *Applied computational geometry towards geometric engineering*. Springer, 1996, pp. 203–222.
[45] M. Chai, L. Luo, K. Sunkavalli, N. Carr, S. Hadap, and K. Zhou, "High-quality hair modeling from a single portrait photo," *ACM Trans. Graph.*, vol. 34, no. 6, pp. 204:1–204:10, Oct. 2015.

Yizhong Zhang is a Ph.D. student in the state key laboratory of CAD&CG, Zhejiang University, Hangzhou, China. He received his B.S. degree in Mechatronics Engineering from Zhejiang University in 2010. His research interests include physically based simulation, computer graphics, computational fabrication and robotics.

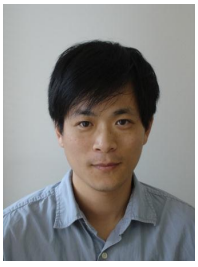

Yiying Tong is an associate professor at Michigan State University. He received his Ph.D. degree from University of Southern California in 2004. His research interests include discrete geometric modeling, physically-based simulation/animation, and discrete differential geometry. He received the U.S. National Science Foundation (NSF) Career Award in 2010.

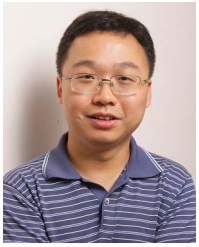

Kun Zhou is a Cheung Kong Professor in the Computer Science Department of Zhejiang University, and the Director of the State Key Lab of CAD&CG. Prior to joining Zhejiang University in 2008, Dr. Zhou was a Leader Researcher of the Internet Graphics Group at Microsoft Research Asia. He received his B.S. degree and Ph.D. degree in computer science from Zhejiang University in 1997 and 2002, respectively. His research interests are in visual computing, parallel computing, human computer interaction, and virtual reality. He currently serves on the editorial/advisory boards of ACM Transactions on Graphics and IEEE Spectrum. He is a Fellow of IEEE.